

1 INTRODUCTION

2 Above Earth's atmosphere are the Van Allen radiation belts, a toroidally-shaped
3 pair of belts that consist of a complex and dynamic plasma environment. The inner
4 radiation belt consists of mostly energetic protons, is very stable on year time scales,
5 and is located within 2 Earth radii (measured near the equator) above Earth's Earth's
6 surface. The outer radiation belt, on the other hand, consists of mostly energetic
7 electrons, is highly dynamic on day, and even hour time scales, and is typically
8 found between 4 and 8 Earth radii above Earth's surface. The radiation belts pose a
9 challenge to space exploration due to their effects on our technology-driven society.
10 Some of the effects include: a higher radiation dose for astronauts and cosmonauts,
11 degradation of silicon to the point where transistors malfunction, computer memory
12 corrupts due to bit flips, etc. With these effects in mind, it is no surprise that the
13 radiation belts have been extensively studied since their discovery in the 1960s.

14 The radiation belt plasma is at times unstable which in turn generate electric and
15 magnetic waves. These waves in turn accelerate and scatter radiation belt particles
16 with a variety of wave-particle mechanisms. One form of wave-particle interactions
17 scatter particles into Earth's atmosphere in the form of electron microbursts.

18 Electron microbursts, henceforth referred to as microbursts, are typically
19 observed by low Earth orbiting spacecraft, sounding rockets, and high altitude
20 balloons as a sub-second impulse of electrons. Some of the most intense microbursts
21 have electron fluxes that are a factor of 10 to 100 above the background (for example
22 see Fig. 7 in Blake et al. (1996)). Since they were first reported by Anderson and
23 Milton (1964), the intense transient nature of microbursts have compelled countless
24 researchers to understand their properties, their effects on the environment, and the
25 physical mechanism(s) that create microbursts. Microbursts are widely believed

²⁶ to be created by wave-particle scattering between a plasma wave called whistler
²⁷ mode chorus and outer radiation belt electrons, although many details regarding the
²⁸ scattering mechanism are unconstrained or unknown. The goal of this dissertation is
²⁹ to study the wave-particle scattering mechanism that scatters electron microbursts.

³⁰ This chapter serves as an introduction to the fundamental physical concepts
³¹ that are essential to understand wave-particle interactions in Earth's magnetosphere.
³² We will first derive the motion of individual charged particles in Earth's electric and
³³ magnetic fields. Next we will cover how various groups of charged particles coalesce
³⁴ to form the major particle populations in the magnetosphere. Then, we will cover
³⁵ the various mechanisms that accelerate and scatter particles in the magnetosphere.
³⁶ Lastly, we will review the basics of microbursts as a jumping-off point for the rest of
³⁷ the dissertation.

³⁸ Charged Particle Motion in Electric and Magnetic Fields

A charged particle trapped in the magnetosphere will experience three types of periodic motion in Earth's nearly dipolar magnetic field. The three motions are ultimately due to the Lorentz force that a particle of momentum \vec{p} , charge q , and velocity \vec{v} experiences in an electric field \vec{E} and magnetic field \vec{B} and is given by

$$\frac{d\vec{p}}{dt} = q(\vec{E} + \vec{v} \times \vec{B}). \quad (1.1)$$

³⁹ In the magnetosphere, the three periodic motions, in decreasing frequency, are
⁴⁰ gyration, bounce, and drift and are schematically shown in Fig. 1.1. Each periodic
⁴¹ motion has a corresponding conserved quantity i.e. an adiabatic invariant.

The highest frequency periodic motion is gyration about a magnetic field of

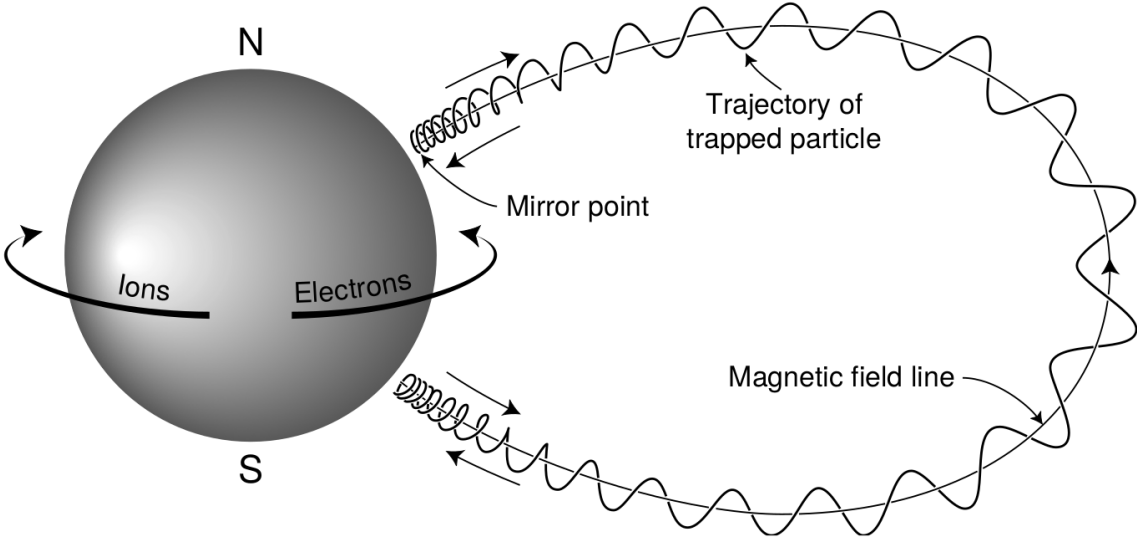


Figure 1.1: The three periodic motions of charged particles in Earth's dipole magnetic field. These motions are: gyration about the magnetic field line, bounce motion between the magnetic poles, and azimuthal drift around the Earth. Figure from (Baumjohann and Treumann, 1997).

magnitude B . This motion is circular with a Larmor radius of

$$r = \frac{mv_{\perp}}{|q|B} \quad (1.2)$$

where m is the mass and v_{\perp} the particle's velocity perpendicular to \vec{B} . This motion has a corresponding gyrofrequency

$$\Omega = \frac{|q|B}{m} \quad (1.3)$$

in units of radians/second. In the radiation belts, the electron gyrofrequency, Ω_e is on the order of a kHz. The corresponding adiabatic invariant is found by integrating the particle's canonical momentum around the particle's path of gyration

$$J_i = \oint (\vec{p} + q\vec{A}) \cdot d\vec{l} \quad (1.4)$$

42 where J_i is the i^{th} adiabatic invariant and \vec{A} is the magnetic vector potential. This
 43 integral is carried out by integrating the first term over the circumference of the
 44 gyro orbit and integrating the second term using Stokes theorem to calculate the
 45 magnetic flux enclosed by the gyro orbit. The gyration invariant is $J_1 \sim v_{\perp}^2/B$, which
 46 is conserved when the frequency, ω of a force acting on the gyrating electron satisfies
 47 $\omega \ll \Omega_e$.

48 The second highest frequency periodic motion is bouncing due to a parallel
 49 gradient in \vec{B} . This periodic motion naturally arises in the magnetosphere because
 50 Earth's magnetic field is stronger near the poles, and artificially in the laboratory
 51 in magnetic bottle machines. To understand this motion we first we need to define
 52 the concept of pitch angle, α as the angle between \vec{B} and \vec{v} which is schematically
 53 shown in Fig. 1.2a. The pitch angle relates v with v_{\perp} , and v_{\parallel} (the component of the
 54 particles velocity parallel to \vec{B}). As shown in Fig. 1.2b and 1.2c, a smaller (larger)
 55 α will increase (decrease) the distance that the charged particle travels parallel to \vec{B} ,
 56 during one gyration.

Assuming the particle's kinetic energy is conserved, the conservation of J_1
 implies that given a particle's $v_{\perp}(0)$ and $B(0)$ at the magnetic equator (where
 Earth's magnetic field is usually at a minimum), we can calculate its $v_{\perp}(s)$ along the
 particle's path s by calculating $B(s)$ from magnetic field models. Thus the particle's
 perpendicular velocity is then related via

$$\frac{v_{\perp}^2(0)}{B(0)} = \frac{v_{\perp}^2(s)}{B(s)} \quad (1.5)$$

57 which can be rewritten as

$$\frac{v^2 \sin^2 \alpha(0)}{B(0)} = \frac{v^2 - v_{\parallel}^2(s)}{B(s)} \quad (1.6)$$

⁵⁸ and re-arranged to solve for $v_{||}(s)$

$$v_{||}(s) = v \sqrt{1 - \frac{B(s)}{B(0)} \sin^2 \alpha(0)} \quad (1.7)$$

⁵⁹ which will tend towards 0 when the second term in the radical approaches 1.

⁶⁰ The location where $v_{||}(s) = 0$ is called the mirror point and is where a particle
⁶¹ reverses direction. Since Earth's magnetic field is stronger towards the poles, the
⁶² mirroring particle will execute periodic bounce motion between its two mirror points
⁶³ in the northern and southern hemispheres. The corresponding adiabatic invariant, J_2
⁶⁴ is

$$J_2 = \oint p_{||} ds \quad (1.8)$$

where ds describes the particle path between the mirror points in the northern and southern hemispheres (see Fig. 1.1). J_2 is found by substituting Eq. 1.7 into Eq. 1.8 and defining the magnetic field strength at the mirror points as B_m (where $\alpha(m) = 90^\circ$). The J_2 integral can be written as

$$J_2 = 2p \int_{m_n}^{m_s} \sqrt{1 - \frac{B(s)}{B(m)}} ds \quad (1.9)$$

⁶⁵ where m_n and m_s are the northern and southern mirror points, respectively. The
⁶⁶ bounce period can be estimated (e.g. Baumjohann and Treumann, 1997) to be

$$t_b \approx \frac{LR_e}{\sqrt{W/m}} (3.7 - 1.6 \sin \alpha(0)) \quad (1.10)$$

⁶⁷ where W is the particle's kinetic energy, and L is the L -shell. L -shell describes the
⁶⁸ distance from the Earth's center to the location where a particular magnetic field
⁶⁹ line crosses the magnetic equator, in units of Earth radii, R_e . As with gyration, the

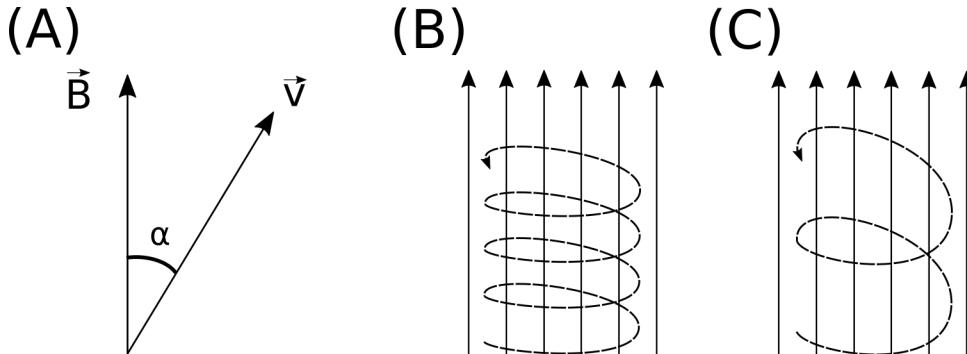


Figure 1.2: Charged particle motion in a uniform magnetic field \vec{B} . Panel (A) shows the geometry defining the pitch angle, α . Panel (B) and (C) show two helical electron trajectories with dashed lines assuming a large and small α (corresponding to a small and large parallel velocity $v_{||}$), respectively.

70 particle will bounce between the mirror points as long as $\omega \ll \Omega_b$, where Ω_b is the
71 bounce frequency.

72 At this stage it is instructional to introduce the notion of the loss cone pitch
73 angle, α_L . A particle with $\alpha \leq \alpha_L$ will mirror at or below ≈ 100 km altitude in
74 the atmosphere. A charged particle gyrating at those altitudes will encounter and
75 Coulomb scatter with the dense atmosphere and be lost from the magnetosphere.

76 The slowest periodic motion experienced by charged particles in Earth's mag-
77 netic field is azimuthal drift around the Earth. This drift results from a combination of
78 a radial gradient in \vec{B} and the curvature of the magnetic field. The radial gradient drift
79 arises because Earth's magnetic field is stronger near the Earth where the particle's
80 gyroradius radius of curvature shrinks as it gyrates towards stronger magnetic field,
81 and expands when it gyrates outward. The overall effect is the particle gyro orbit does
82 not close on itself and negatively charged particles drift east and positively charged
83 particles drift west. The radial gradient drift is further enhanced by the centrifugal
84 force that a particle experiences as it bounces along the curved field lines. The drift
85 adiabatic invariant, J_3 is found by integrating Eq. 1.4 over the complete particle orbit

86 around the Earth. The shape of this drift orbit is known as a drift shell. For J_3 , the
 87 first term is negligible and the second term is the magnetic flux enclosed by the drift
 88 shell, Φ_m i.e. $J_3 \sim \Phi_m$.

89 Figure 1.3 from Schulz and Lanzerotti (1974) shows contours of the gyration,
 90 bounce, and drift frequencies for electrons and protons in Earth's dipole magnetic
 91 field.

Up until now we have considered the three periodic motions due Earth's magnetic field in the absence of electric fields. If there is an electric field, E_\perp perpendicular to \vec{B} , a particle's center of gyration i.e., averaged position of the particle over a gyration, will drift with a velocity perpendicular to both E_\perp and \vec{B} . The drift velocity can be solved using Eq. 1.1 and is

$$\vec{v}_E = \frac{\vec{E} \times \vec{B}}{B^2}. \quad (1.11)$$

92 If there is a parallel magnetic field, $E_{||}$ then the particle is accelerated along the
 93 magnetic field line. An $E_{||}$ pointing away from the Earth will contribute to the mirror
 94 force and raise the particle's mirror point. On the contrary, an Earthward pointing
 95 $E_{||}$ will oppose the mirror force and lower the mirror point. If the Earthward $E_{||}$ is
 96 strong enough, the mirror point is lowered into the atmosphere that will precipitate
 97 particles. This is the mechanism that generates the aurora.

98 Particle Populations and Their Interractions in the Magnetosphere

99 Now that we have looked at the dynamics of single-particle motion in electric
 100 and magnetic fields, we will briefly tour the various macroscopic populations in the
 101 magnetosphere that are illustrated in Fig. 1.4.

102 The sun and its solar wind are ultimately the source of energy input into the
 103 magnetosphere. The solar wind at Earth's orbit is a plasma traveling at supersonic

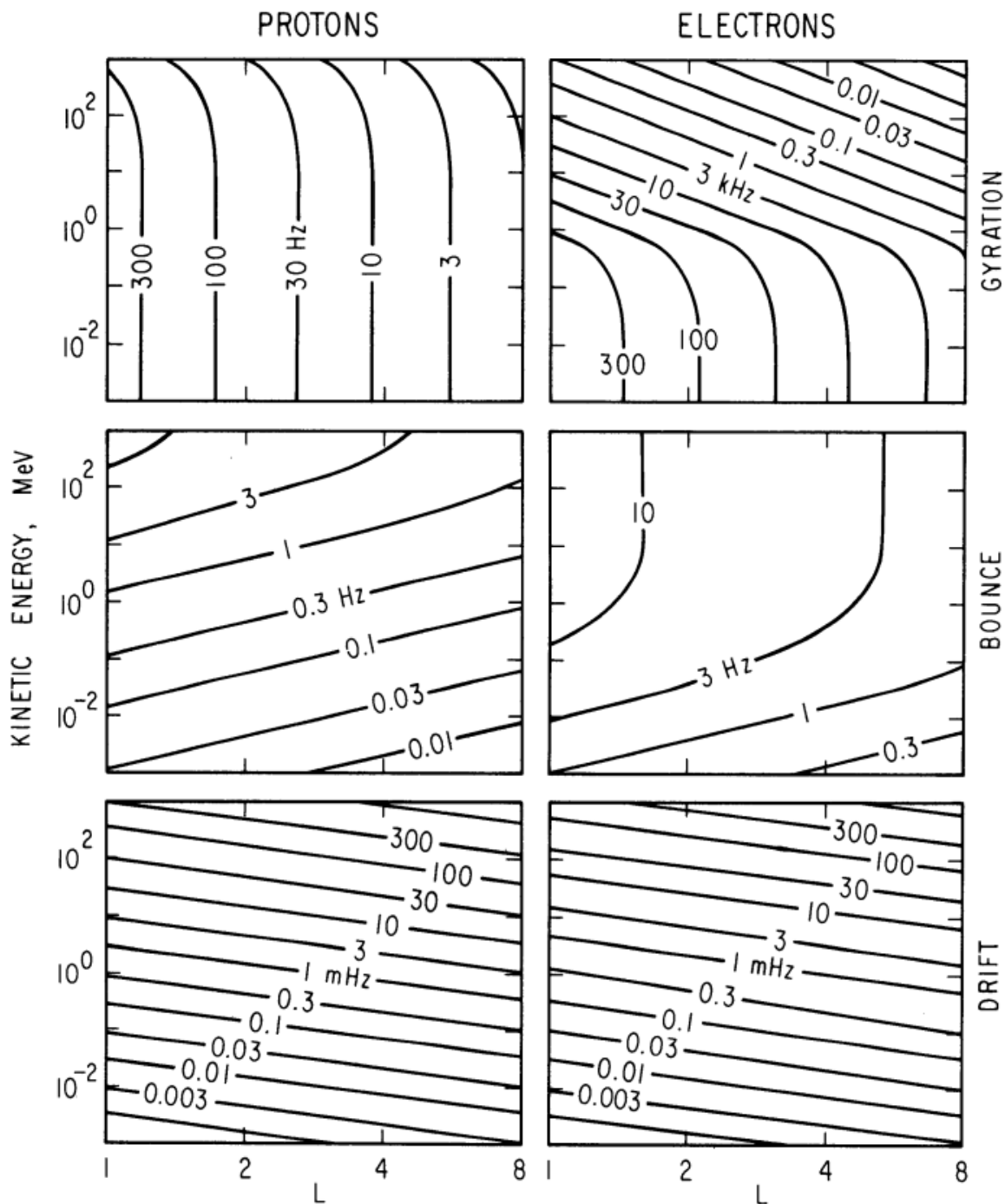


Figure 1.3: Contours of constant gyration, bounce, and drift frequencies for electrons and protons in a dipole field. Figure from Schulz and Lanzerotti (1974).

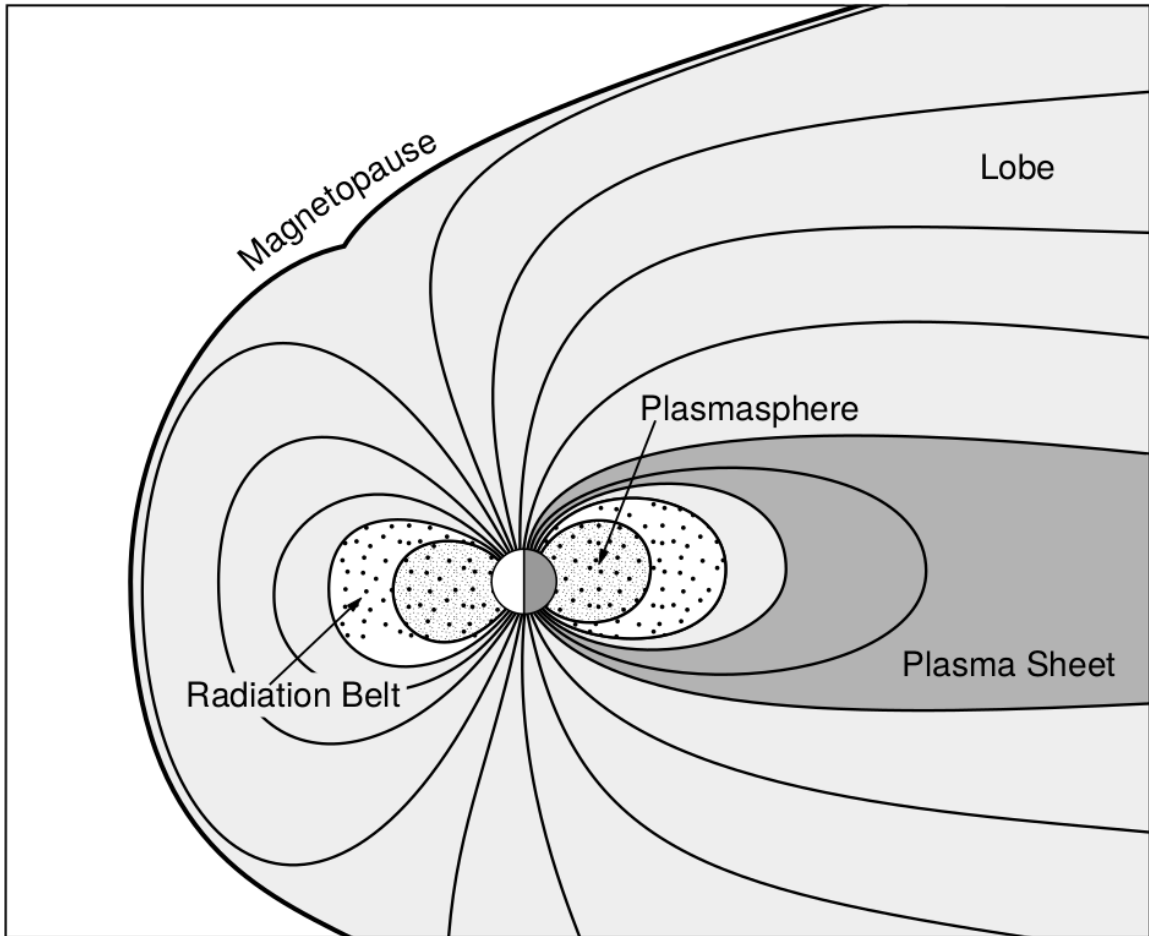


Figure 1.4: A few macroscopic structures in the magnetosphere. The magnetosphere boundary with the solar wind is the magnetopause. The magnetotail consists of two lobes that contain Earth's magnetic flux with the plasma sheet separating the two lobes. The inner magnetosphere contains the plasmasphere, the ring current, and the radiation belts which are co-located. Figure from Baumjohann and Treumann (1997).

speeds with an embedded interplanetary magnetic field (IMF). When the solar wind encounters Earth's magnetic field, the plasma can not easily penetrate into the magnetosphere because the plasma is frozen-in on magnetic field lines. Thus the plasma and its magnetic field drapes around the magnetosphere, forming a cavity in the solar wind that qualitatively has a shape as shown in Fig. 1.4. Because the solar wind is supersonic at 1 AU, a bow shock exists upstream of the magnetosphere. The solar wind plasma, after it is shocked by the bow shock, flows around the magnetosphere inside the magnetosheath. The surface where the solar wind ram pressure and Earth's magnetic pressure balance is termed the magnetopause, which can be thought of as a boundary between the solar wind and Earth's magnetosphere. This is a slightly naive description of the magnetopause, but is nonetheless an instructive conceptual picture. The shocked plasma then flows past the Earth where it shapes the magnetotail. In the magnetotail the magnetopause exists where the solar wind magnetic pressure balances Earth's magnetic field pressure in the lobes. The magnetotail extends on the order of $100 R_E$ downstream of Earth, and the tailward stretching of magnetic field lines creates the plasma sheet which exists in the region of low magnetic field strength near the magnetic equator (e.g. Eastwood et al., 2015).

121 Populations in the Inner Magnetosphere

Closer to Earth, where the magnetic field is largely dipolar, are three plasma populations that comprise the inner magnetosphere: the plasmasphere, the ring current, and the radiation belts which are shown in Fig. 1.4. Before we describe these three particle populations in detail, we will first introduce the coordinate system that most naturally describes the inner magnetosphere environment, and then the electric fields that effect mostly low energy particles.

In this coordinate system the “radial” coordinate was defined in section 1 and

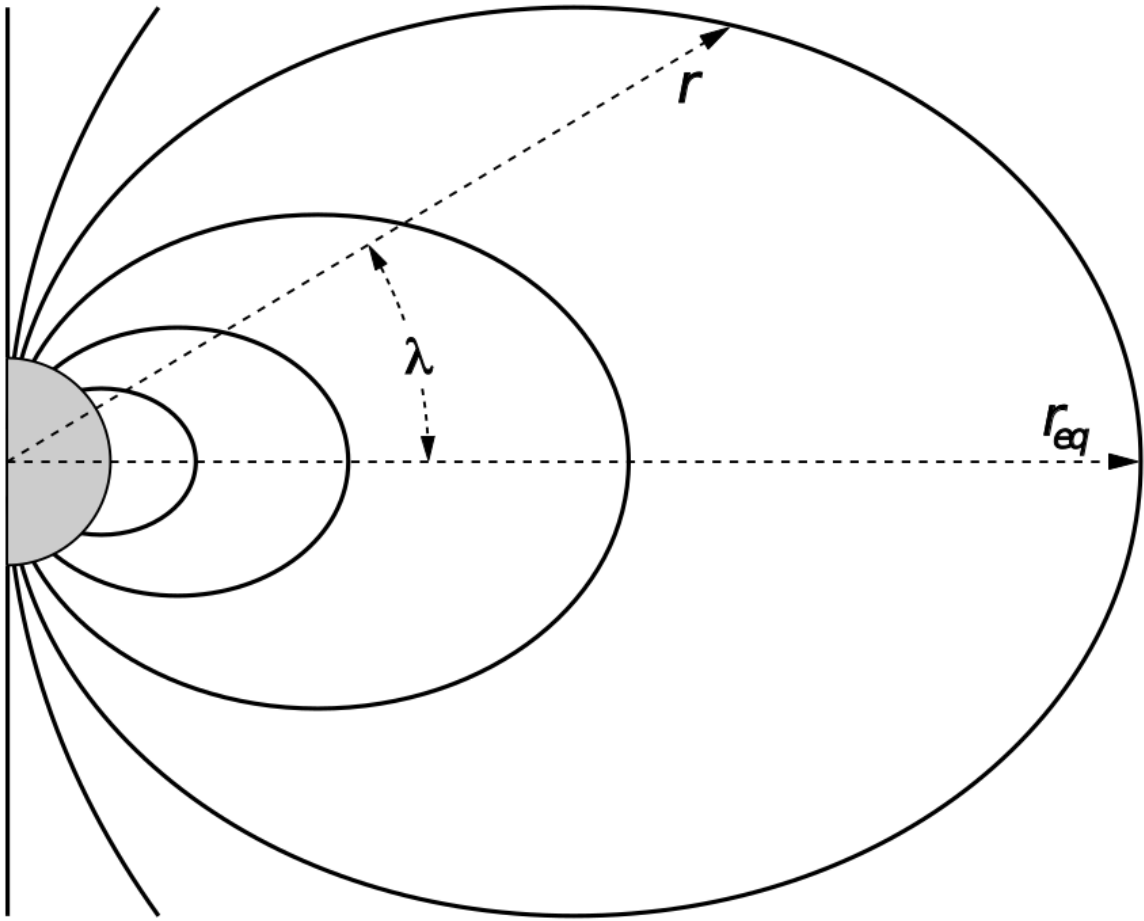


Figure 1.5: The dipole coordinate system. The magnetic latitude of \mathbf{r} is λ . The radial distance to a magnetic field line in the equatorial plane is typically given by $L = r_{eq}/R_e$. Figure from Baumjohann and Treumann (1997).

is the L shell. The azimuthal coordinate is the magnetic local time (MLT). For an observer above Earth's north pole looking down, MLT is defined to be 0 (midnight) in the anti-sunward direction, and increases in the counter-clockwise direction with 6 at dawn, 12 at noon (sunward direction), and 18 in dusk. The final coordinate is the magnetic latitude, λ which is analogous to the latitude coordinate in the spherical coordinate system, and is defined to be 0 at the magnetic equator. This coordinate system is shown in Fig. 1.5 and naturally describes the inner magnetosphere populations described below.

137 The low energy particle dynamics in the inner magnetosphere are organized by
 138 two electric fields: the co-rotation and the dawn-dusk electric fields. The co-rotation
 139 electric field arises from Earth's rotation. The magnetic field and the particles frozen
 140 on it rotate with the Earth. To a non-rotating observer this rotation appears as a
 141 radial electric field that drops off as $\sim L^{-2}$. The other electric field, pointing from
 142 dawn to dusk is called the convection electric field and is due to the Earthward
 143 transport of particles from the magnetotail that appears as an electric field in Earth's
 144 reference frame. The superposition of the co-rotation and convection electric
 145 fields is a potential field shown in Fig. 1.6. The shaded area in Fig. 1.6 shows the
 146 orbits on which low energy electrons are trapped, and outside this region the particles
 147 are not trapped. The dynamic topology of the shaded region in Fig. 1.6 is controlled
 148 by only the convection electric field which is dependent on the solar wind speed and
 149 the IMF. The lowest energy particles that orbit in the shaded region in Fig. 1.6 make
 150 up the plasmasphere.

151 Plasmasphere The plasmasphere is a dense ($n_e \sim 10^3/\text{cm}^3$), cool plasma
 152 ($\sim \text{eV}$) that extends to $L \sim 4$ (extent is highly dependent on the solar wind and
 153 magnetospheric conditions) and is sourced from the ionosphere. The two main
 154 mechanisms that source the cold plasma from the ionosphere are ultraviolet ionization
 155 by sunlight and particle precipitation. The ultraviolet ionization by sunlight is
 156 strongly dependent on the time of day (day vs night), latitude (more ionization near
 157 the equator). The ionization due to particle precipitation, on the other hand, is highly
 158 dependent on magnetospheric conditions, and mostly occurs at high latitudes.

159 The outer boundary of the plasmasphere is the plasmapause which is typically
 160 identified as a steep radial gradient in plasma density from $\sim 10^3/\text{cm}^3$ to $\sim 1/\text{cm}^3$. As
 161 we will see throughout this dissertation, the location of the plasmapause is important

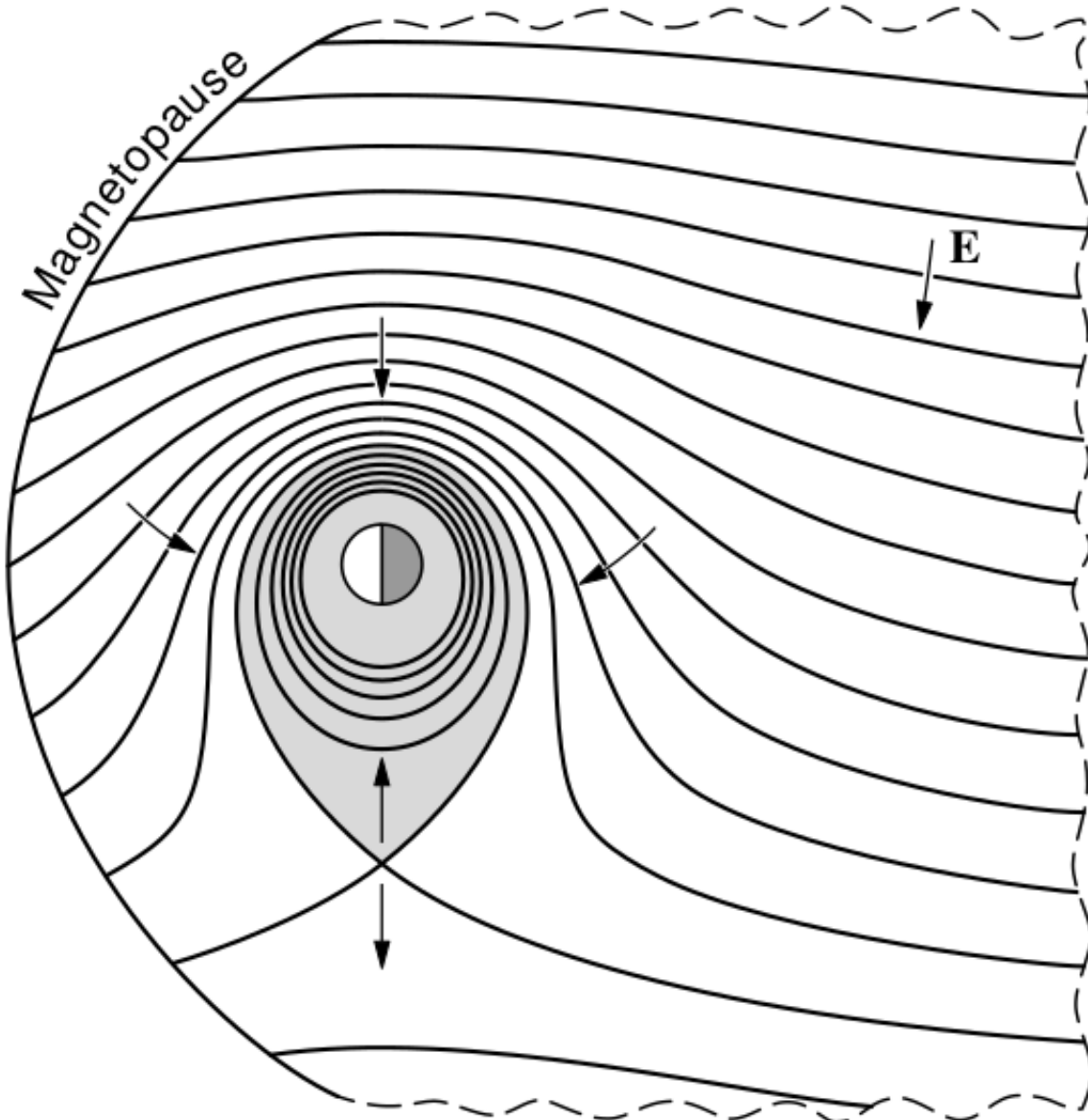


Figure 1.6: Equipotential lines and electric field arrows due to the superposition of the co-rotation and convection electric fields. Electrons in the shaded region execute closed orbits. Outside of the shaded regions the electrons are not trapped and will escape. The region separating the two regimes is called the Alfvén layer. Figure from Baumjohann and Treumann (1997).

₁₆₂ to model (e.g. O'Brien and Moldwin, 2003) and understand since the plasma density
₁₆₃ strongly controls the efficiency of particle scattering (Horne et al., 2005).

₁₆₄ Ring Current The next higher energy population is the ring current. This
₁₆₅ population consists of protons and electrons between tens and a few hundred keV
₁₆₆ that drift around the Earth. The orbits of higher energy particles are not as effected
₁₆₇ by the convection and co-rotation electric field, rather they drift around the Earth
₁₆₈ due to gradient and curvature drifts. Since the direction of the drift is dependent on
₁₆₉ charge, protons drift west around the Earth and electrons drift East. This has the
₁₇₀ effect of creating a current around the Earth.

₁₇₁ The ring current generates a magnetic field which decreases the magnetic field
₁₇₂ strength on Earth's surface and increases it outside of the ring current. The decrease
₁₇₃ of Earth's magnetic field strength is readily observed by a system of ground-based
₁₇₄ magnetometers and is merged into a Disturbance Storm Time (DST) index. An
₁₇₅ example of a DST index time series from a coronal mass ejection (CME) driven 2015
₁₇₆ St. Patrick's Day storm is shown in Fig. 1.7. The ring current is sometimes first
₁₇₇ depleted and DST increases slightly (initial phase or sudden storm commencement).
₁₇₈ Then the ring current is rapidly built up during which DST rapidly decreases (main
₁₇₉ phase). Lastly the ring current gradually decays toward its equilibrium state over a
₁₈₀ period of a few days and DST increases towards 0 (recovery phase). The DST index
₁₈₁ along with other indicies are readily used by the space physics community to quantify
₁₈₂ the global state of the magnetosphere.

₁₈₃ Radiation Belts The highest energy particle populations are in the Van Allen
₁₈₄ radiation belts. These belts were discovered by Van Allen (1959) and Vernov and
₁₈₅ Chudakov (1960) during the Cold War and are a pair of toroidally shaped populations
₁₈₆ of trapped electrons and protons usually within to $L < 8$ and are shown in Fig. 1.8.

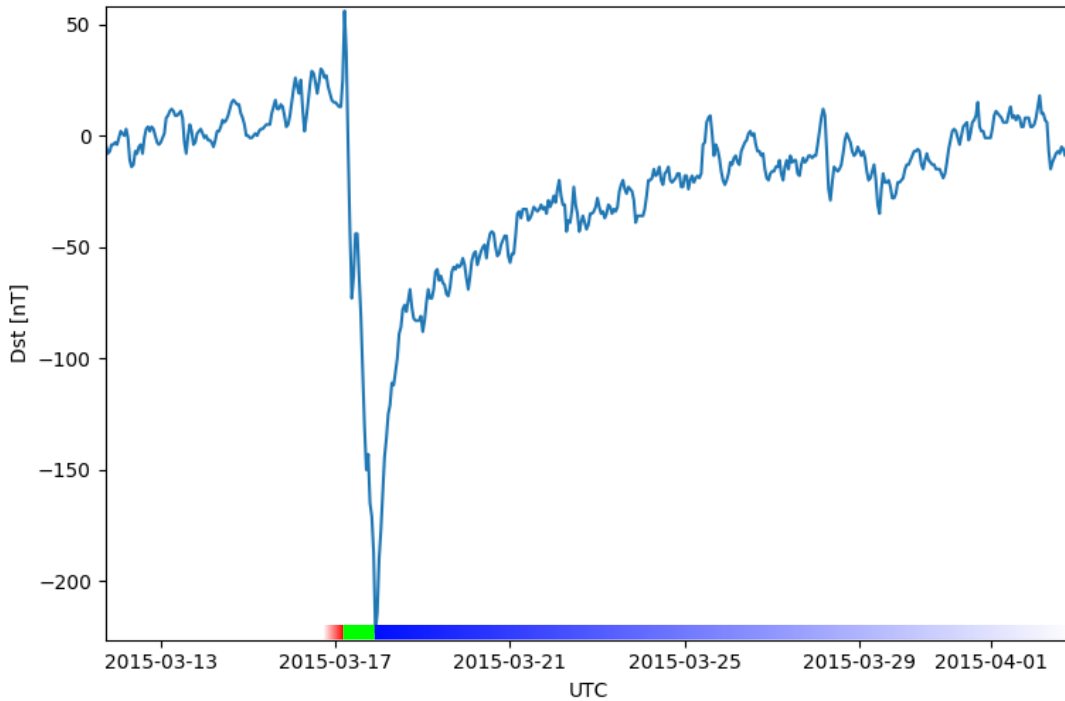


Figure 1.7: The DST index during the St. Patrick's Day 2015 storm. This storm was caused by a coronal mass ejection on March 15th, 2015. The storm phases are: initial phase, main phase, and recovery phase. The initial phase occurred when the Dst peaked at +50 nT on March 17th during which the ring current was eroded by the coronal mass ejection during the interval shown by the red bar. Then the rapid decrease to ≈ -200 nT was during the main phase where many injections from the magnetotail pumped up the ring current which reduced Earth's magnetic field strength at the ground and is shown with the green bar. Lastly, the recovery phase lasted from March 18th to approximately March 29th during which the ring current particles were lost and the ring current returned to its equilibrium state. The recovery phase is shown with the blue bar.

The Earth's Electron Radiation Belts

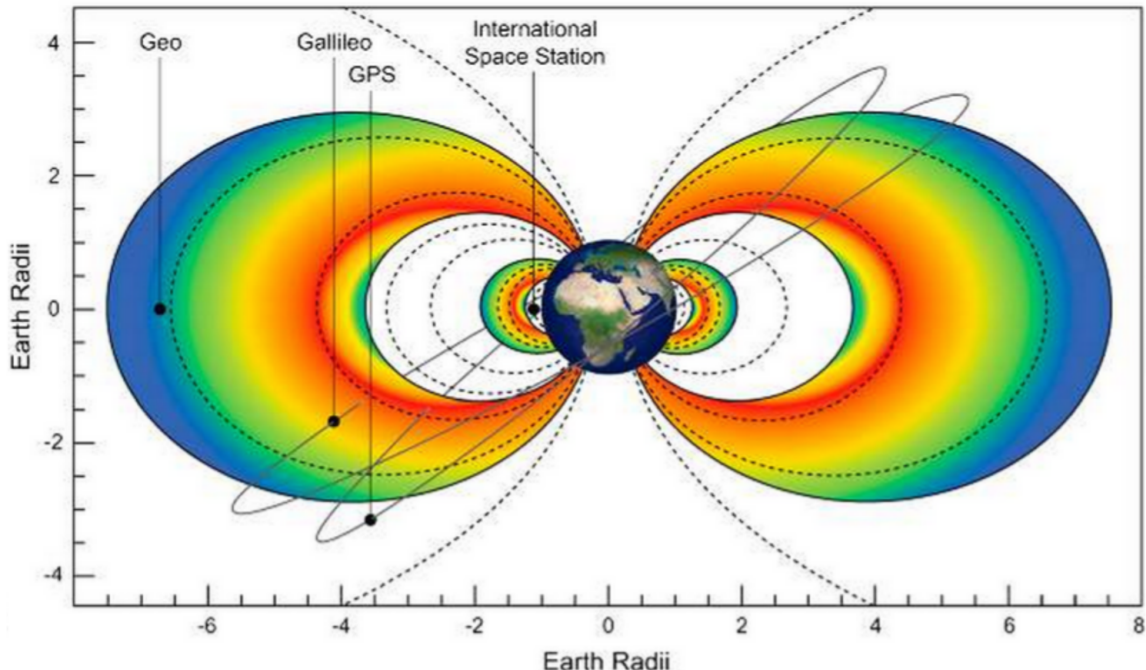


Figure 1.8: The two radiation belts with the locations of various satellites and orbits. Figure from (Horne et al., 2013).

187 Their quiescent toroidal shape is similar to the shape of the plasmasphere and ring
 188 current and is a result of Earth's dipole magnetic field and the conservation of the
 189 three adiabatic invariants discussed in section 1.

190 The inner radiation belt is extremely stable on time periods of years, extends
 191 to $L \approx 2$, and mainly consists of protons with energies between MeV and GeV and
 192 electrons with energies up to ≈ 1 MeV (Claudepierre et al., 2019). The source of
 193 inner radiation belt protons is believed to be due to cosmic-ray albedo neutron decay
 194 (e.g. Li et al., 2017) and inward radial diffusion for electrons (e.g. O'Brien et al.,
 195 2016). The gap between the inner and outer radiation belt is called the slot, which is
 196 believed to be due to hiss waves inside the plasmasphere (described below) scattering
 197 particles into the atmosphere (e.g. Breneman et al., 2015; Lyons and Thorne, 1973).

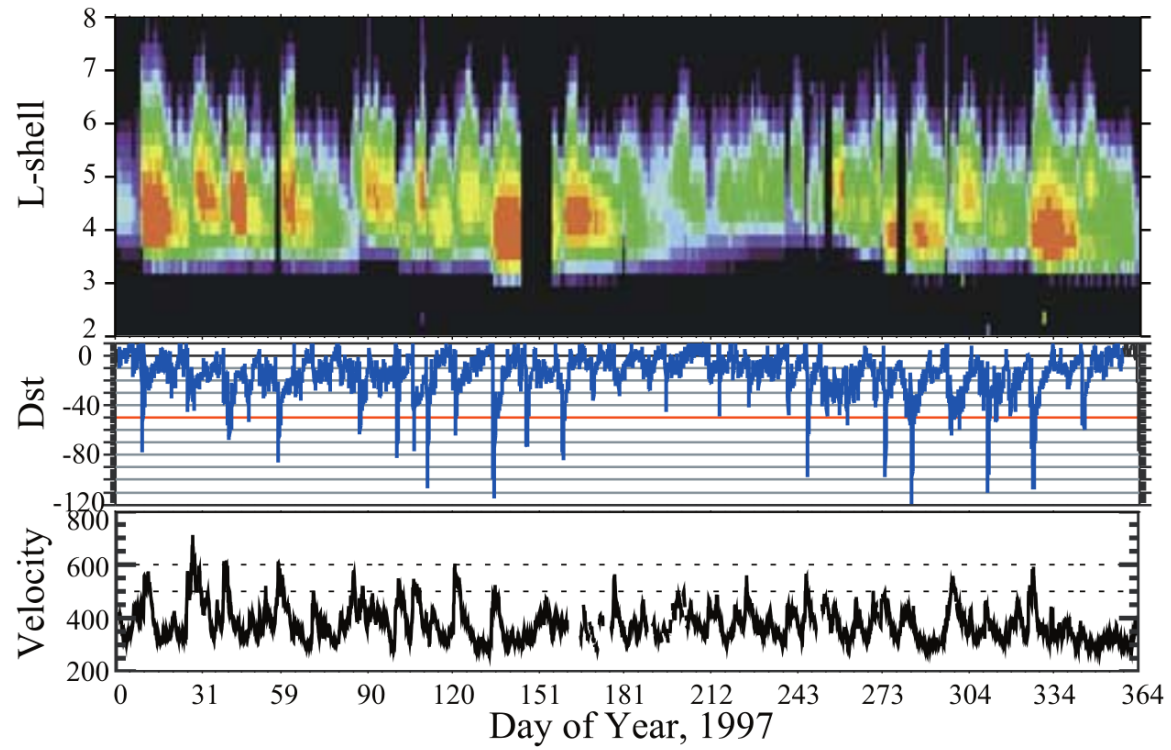


Figure 1.9: The dynamics of the outer radiation belt in 1997 from the POLAR satellite. Top panel shows the 1.2-2.4 MeV electron flux as a function of L and 1997 day of year. The middle panel shows the DST index, and bottom panel shows the solar wind velocity. Figure from (Reeves et al., 2003).

198 The outer radiation belt, on the other hand is much more dynamic and consists
 199 of mainly electrons of energies up to a few MeV. The outer belt's spatial extent is
 200 highly variable e.g. see Fig. 1.9, and is typically observed at $4 < L < 8$. Since
 201 the outer radiation belt contains a dynamic population of energetic particles that
 202 pose a threat to human and technological presence in Earth's atmosphere and space,
 203 decades of research has been undertaken to understand and predict the outer radiation
 204 belt particles, waves, and wave-particle interactions. The dynamics of the outer
 205 radiation belt can be understood by considering various competing acceleration and
 206 loss mechanisms which will be described in the following sections.

207 Radiation Belt Particle Sources and Sinks

208 Adiabatic Heating

209 One of the particle heating and transport mechanisms arises from the Earthward
 210 convection of particles. The conservation of J_1 implies that the initial and final v_\perp
 211 depends on the change in the magnetic field amplitude

$$\frac{v_{\perp i}^2}{B_i} = \frac{v_{\perp f}^2}{B_f}. \quad (1.12)$$

212 As a particle convets Earthward, $B_f > B_i$ thus v_\perp must increase. The dipole
 213 magnetic field amplitude can be written as

$$B(L, \theta) = \frac{31.2 \mu\text{T}}{L^3} \sqrt{1 + 3 \cos^2 \theta} \quad (1.13)$$

214 which implies that

$$\frac{v_{\perp f}^2}{v_{\perp i}^2} = \left(\frac{L_i}{L_f} \right)^3. \quad (1.14)$$

215 .

216 In addition, as the particle convects Earthward the distance between the
 217 particle's mirror points decrease. If J_2 is conserved, the shrinking bounce path implies
 218 that v_{\parallel} must increase by

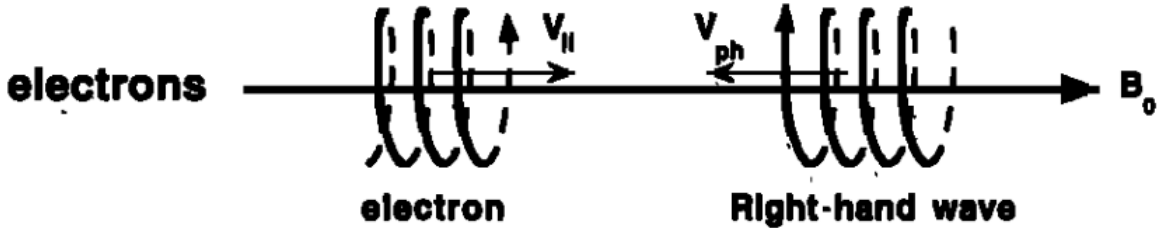
$$\frac{v_{\parallel f}^2}{v_{\parallel i}^2} = \left(\frac{L_i}{L_f}\right)^k \quad (1.15)$$

219 where k ranges from 2 for equatorial pitch angles, $\alpha_{eq} = 0^\circ$, to 2.5 for $\alpha_{eq} = 90^\circ$
 220 (Baumjohann and Treumann, 1997). Since the rate of adiabatic heating is greater in
 221 the perpendicular direction than heating in the parallel direction, an initially isotropic
 222 particle distribution will become anisotropic during its convection. These isotropic
 223 particles can then become unstable to wave growth and generate waves in order to
 224 reach equilibrium.

225 Wave Resonance Heating

226 Another mechanism that heats particles is due to particles resonating with
 227 plasma waves. A few of the electromagnetic wave modes responsible for particle
 228 acceleration (and deceleration) relevant to radiation belt dynamics are hiss, whistler
 229 mode chorus (chorus), and electromagnetic ion cyclotron (EMIC) waves. These waves
 230 are created by the loss cone instability that driven by an anisotropy of electrons
 231 for chorus waves, and protons for EMIC waves. The level of anisotropy can be
 232 quantified by the ratio of the perpendicular to parallel particle temperatures (T_{\perp}/T_{\parallel}).
 233 A particle distribution is unstable when $T_{\perp}/T_{\parallel} > 1$ which facilitates wave growth.
 234 Since electrons gyrate in a right-handed sense, the chorus waves also tend to be right
 235 hand circularly polarized (Tsurutani and Lakhina, 1997). The same argument applies
 236 to protons and left hand circularly polarized EMIC waves as well.

237 These circularly polarized waves can resonate with electrons and/or protons



$$\omega + k_{\parallel}v_{\parallel} = \Omega^-$$

Figure 1.10: The trajectories of an electron and a right-hand circularly polarized wave during a cyclotron resonance. The electron's v_{\parallel} and the wave's k_{\parallel} are in opposite directions such that the wave's frequency is Doppler shifted to an integer multiple of the electron cyclotron frequency. Figure from (Tsurutani and Lakhina, 1997).

when their combined motion results in a static \vec{E} . One example of a resonance between a right hand circularly polarized wave and an electron is shown in Fig. 1.21 and is termed the cyclotron resonance. An electron's v_{\parallel} and the wave's parallel wave vector, k_{\parallel} are in opposite directions such that the wave frequency ω is Doppler shifted to an integer multiple of the Ω_e at which point the electron feels a static electric field and is accelerated or decelerated. This acceleration happens when a resonance condition is satisfied between a wave and a particle for which we will now derive an illustrative toy model.

Assume a uniform magnetic field $\vec{B} = B_0\hat{z}$ with a parallel propagating ($k = k\hat{z}$), right-hand circularly polarized wave. The wave's electric field as a function of position and time can be written as

$$\vec{E} = E_0(\cos(\omega t - kz)\hat{x} + \sin(\omega t - kz)\hat{y}) \quad (1.16)$$

which is more clearly expressed by taking the dot product to find \vec{E} in the $\hat{\theta}$ direction

$$E_{\theta} = \vec{E} \times \hat{\theta} = E_0 \cos(\omega t - kz + \theta). \quad (1.17)$$

²⁴⁹ Now assume that the electron is traveling in the $-\hat{z}$ direction with a velocity $\vec{v} = -v_0\hat{z}$
²⁵⁰ so its time dependent position along \hat{z} is

$$z(t) = -v_0 t \quad (1.18)$$

²⁵¹ and gyrophase is

$$\theta(t) = -\Omega t + \theta(0) \quad (1.19)$$

²⁵² where the first negative sign comes from the electron's negative charge. Now we put
²⁵³ this all together and express the electric field and the force that the electron will
²⁵⁴ experience

$$m \frac{dv_\theta}{dt} = qE_\theta = qE_0 \sin((\omega + kv_0 - \Omega)t + \theta(0)). \quad (1.20)$$

²⁵⁵ This is a relatively complex expression, but when the time dependent component,

$$\omega + kv_0 - \Omega = 0, \quad (1.21)$$

²⁵⁶ the electron will be in a static electric field which will accelerate or decelerate the
²⁵⁷ electron depending on θ_0 , the phase between the wave and the electron. **Show Bortnik**
²⁵⁸ **2008 plot?** The expression in Eq. 1.21 is commonly referred to as the resonance
²⁵⁹ condition and is more generally written as

$$\omega - k_{||}v_{||} = \frac{n\Omega_e}{\gamma} \quad (1.22)$$

²⁶⁰ where n is the resonance order, and γ is the relativistic correction (e.g. Millan and
²⁶¹ Thorne, 2007). In the case of the cyclotron resonance, $\omega \approx \Omega_e$ thus J_1 is violated.
²⁶² Since J_1 is violated, J_2 and J_3 are also violated since the conditions required to

263 violate J_2 and J_3 are less stringent than J_1 . It is important to remember that along
 264 the particle's orbit it will encounter and experience the effects of many waves along
 265 its orbit. The typical MLT extent of a handful of waves that are capable of resonating
 266 with radiation belt electrons are shown in Fig. 1.11.

267 Particle Losses

268 Now that we have seen two general mechanisms with which particles are
 269 accelerated and transported in the magnetosphere, we will now consider a few
 270 specific mechanisms with which particles are lost to the atmosphere or the solar
 271 wind. One particle loss mechanism into the solar wind is magnetopause shadowing
 272 (e.g. Ukhorskiy et al., 2006). Particles are sometimes lost when the ring current is
 273 strengthened and Earth's magnetic field strength is increased outside of the ring
 274 current (and reduced on Earth's surface). If the time scale of the ring current
 275 strengthening is slower than a particle drift, J_3 is conserved. Then in order to
 276 conserve J_3 while the magnetic field strength is increased, the particle's drift shell
 277 must move outward to conserve the magnetic flux contained by the drift shell. Then
 278 if the particle's drift shell expands to the point that it crosses the magnetopause, the
 279 particle will be lost to the solar wind.

280 Another particle loss (and acceleration) mechanism is driven by ultra low
 281 frequency (ULF) waves and is called radial diffusion. Radial diffusion is the transport
 282 of particles from high to low phase space density, f . If the transport is radially inward,
 283 particles will appear to be accelerated. On the other hand, radially outward radial
 284 diffusion can transport particles through the magnetopause where they will be lost
 285 to the solar wind. Reeves et al. (2013) investigated the driver of particle acceleration
 286 during the October 2012 storm and observationally found that inward radial diffusion
 287 was not dominant, rather local acceleration via wave-resonance heating (i.e. particle

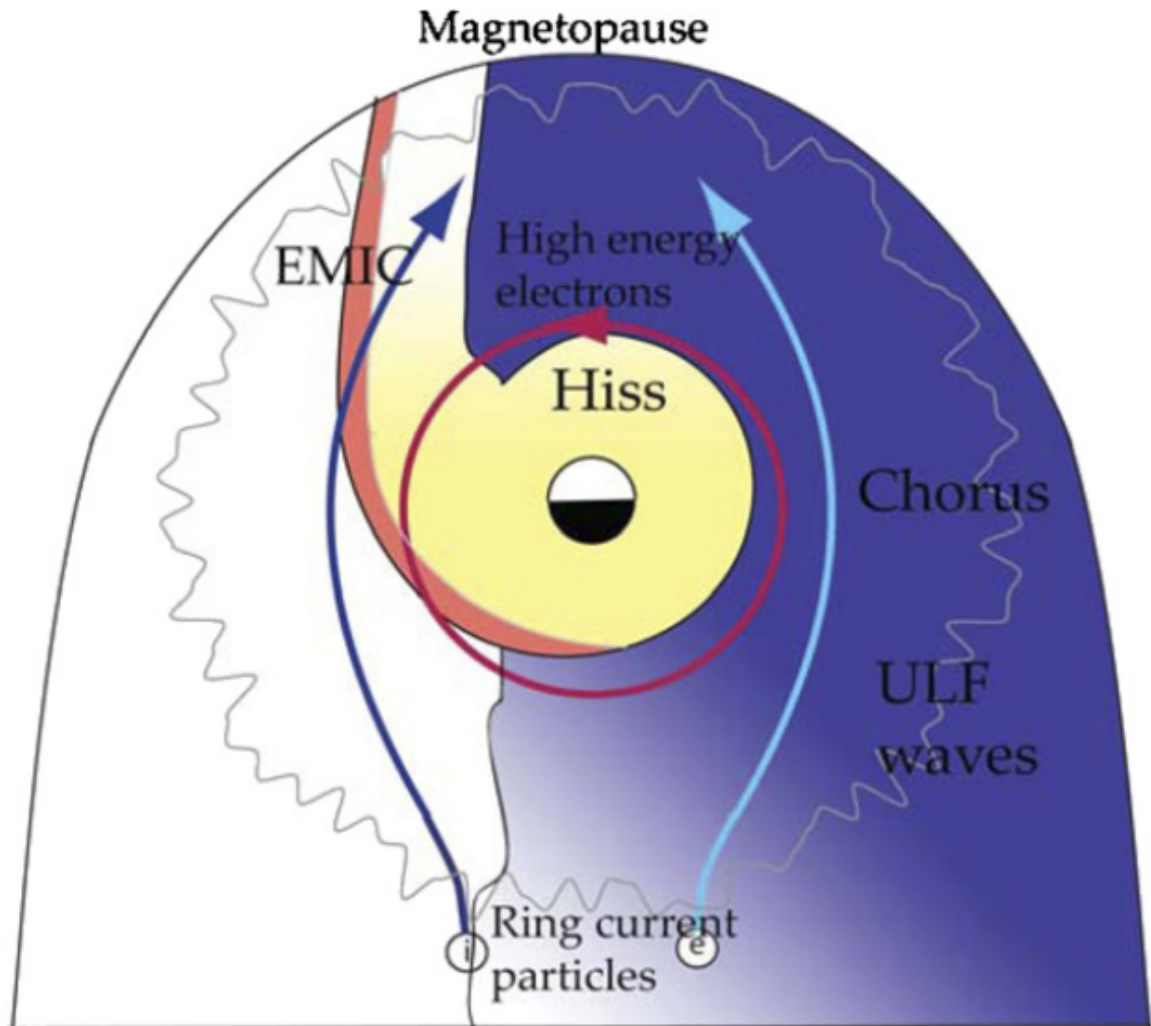


Figure 1.11: Various wave modes in the magnetosphere. Ultra low frequency waves occur through the magnetosphere. Chorus waves are typically observed in the 0-12 midnight-dawn region. EMIC waves are typically observed in the dusk MLT sector. Hiss waves are observed inside the plasmasphere. Figure from Millan and Thorne (2007).

288 diffusion in pitch angle and energy which will be described below) appeared to be the
 289 dominant acceleration mechanism.

290 The loss mechanism central to this dissertation is pitch angle and energy
 291 scattering of electrons by waves. Some of the waves that scatter electrons in energy
 292 and pitch angle in the inner magnetosphere are: plasmaspheric hiss (e.g. Breneman
 293 et al., 2015; O'Brien et al., 2014), EMIC waves (e.g. Capannolo et al., 2019; Hendry
 294 et al., 2017), and chorus waves (e.g. Breneman et al., 2017; Kasahara et al., 2018;
 295 Ozaki et al., 2019). These wave-particle interactions occur when the resonance
 296 condition in Eq. 1.22 is satisfied at which point the particle's energy and α is modified
 297 by the wave. More details regarding the theory of pitch angle and energy diffusion is
 298 given in Chapter X. If the wave changes α towards 0 such that $\alpha < \alpha_{LC}$, the particle's
 299 mirror point lowers to less than 100 km altitude where the particle can be lost due
 300 collisions with air. One manifestation of pitch angle scattering of particles into the
 301 loss cone are microbursts: a sub-second durtaison impulse of electrons.

302 Microbursts

303 Microbursts were first found in high altitude balloon measurements of bremsstrahlung
 304 X-rays emitted by microburst electrons impacting the atmosphere by Anderson
 305 and Milton (1964). In the following years, numerous balloon flights expanded our
 306 knowledge of non-relativistic microbursts (relativistic microbursts have not yet been
 307 observed by high altitude balloons) by quantifying the microburst spatial extent,
 308 temporal width, occurrence frequency, extent in L and MLT, and their source (a
 309 local plasma instability vs. a propagating disturbance in the magnetosphere) (e.g.
 310 Barcus et al., 1966; Brown et al., 1965; Parks, 1967; Trefall et al., 1966). Since then,
 311 non-relativistic and relativistic (> 500 keV) microbursts electrons have been directly
 312 observed in LEO with spacecraft including the Solar Anomalous and Magnetospheric

313 Particle Explorer (SAMPEX) (e.g. Blake et al., 1996; Blum et al., 2015; Douma et al.,
 314 2019, 2017; Greeley et al., 2019; Lorentzen et al., 2001a,b; Nakamura et al., 1995, 2000;
 315 O'Brien et al., 2004, 2003), Montana State University's (MSU) Focused Investigation
 316 of Relativistic Electron Bursts: Intensity, Range, and Dynamics II (FIREBIRD-II)
 317 (Anderson et al., 2017; Breneman et al., 2017; Crew et al., 2016; Klumpar et al.,
 318 2015; Spence et al., 2012), and Science Technologies Satellite (STSAT-I) (e.g. Lee
 319 et al., 2012, 2005). An example microburst time series is shown in Fig. 1.12 and was
 320 observed by the FIREBIRD-II CubeSats. The prominent features of the example
 321 microbursts in Fig. 1.12 are their < 1 second duration, half order of magnitude
 322 increase in count rate above the falling background, and their approximately 200-800
 323 keV energy extent.

324 Microbursts are observed on magnetic field footprints that are connected to the
 325 outer radiation belt (approximately $4 < L < 8$), and are predominately observed in
 326 the 0-12 MLT sector with an elevated occurrence frequency during magnetospherically
 327 disturbed times as shown in Fig. 1.13 (e.g. Douma et al., 2017). O'Brien et al. (2003)
 328 used SAMPEX relativistic electron data and found that microbursts predominately
 329 occur during the main phase of storms, with a heightened occurrence rate during the
 330 recovery phase. Microburst occurrence rates also appear to be higher during high
 331 solar wind velocity events e.g. from co-rotating interaction regions (Greeley et al.,
 332 2019; O'Brien et al., 2003).

333 The impact of microbursts on atmospheric chemistry has been estimated to be
 334 significant. Relativistic microburst electrons impacting the atmosphere are ionized at
 335 < 100 km altitudes, with higher energy electrons penetrating closer to the surface.
 336 The resulting chemical reaction of microburst electrons impacting the atmosphere
 337 produces odd hydrogen HO_x and odd nitrogen NO_x molecules. These molecules are
 338 partially responsible for destroying ozone (O₃). Seppälä et al. (2018) modeled a six

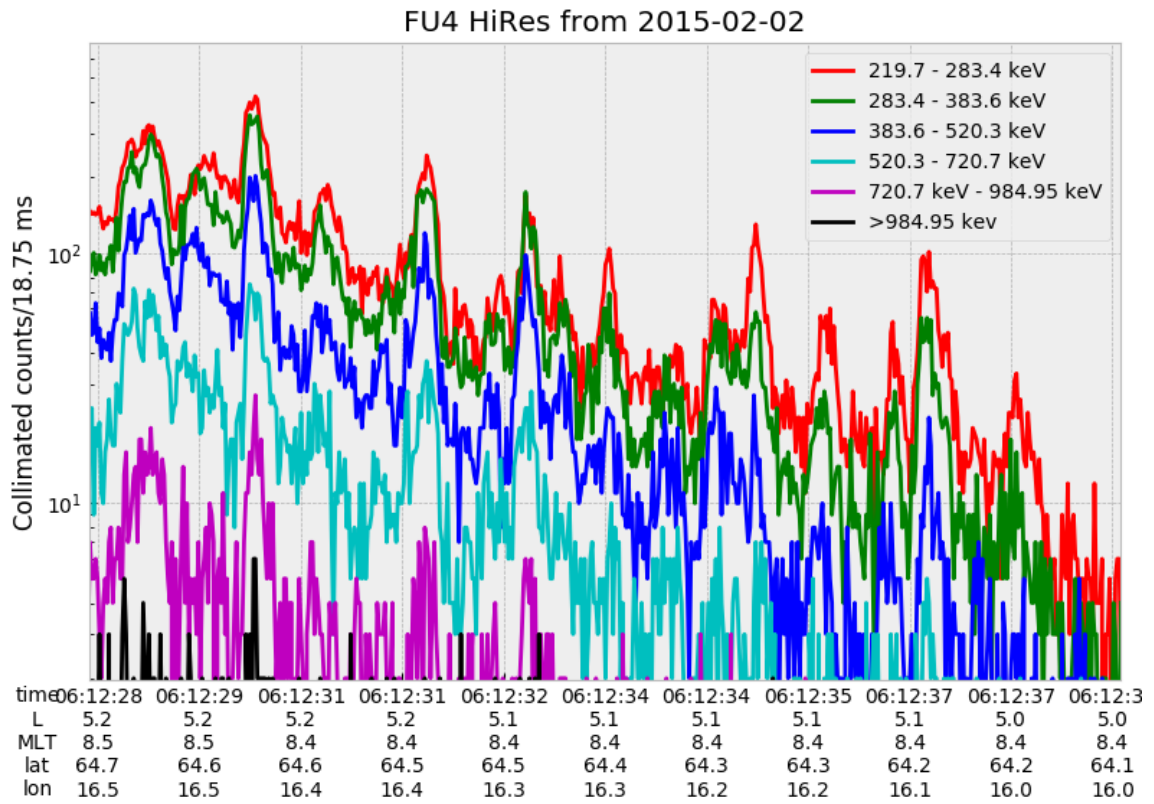


Figure 1.12: An example train of microbursts observed by FIREBIRD-II unit 4 on February 2nd, 2015. The colored curves show the differential energy channel count rates in six channels from ≈ 200 keV to greater than 1 MeV. The x-axis labels show auxiliary information such as time of observation and the spacecraft position in L, MLT, latitude and longitude coordinates.

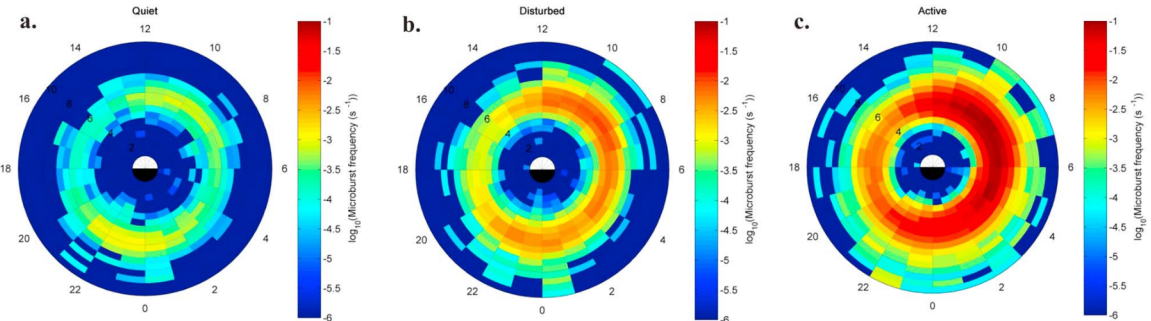


Figure 1.13: Relativistic ($> 1\text{MeV}$) distribution of microburst occurrence rates as a function of L and MLT. The three panels show the microburst occurrence rate dependence on geomagnetic activity, parameterized by the auroral electrojet (AE) index for (a) $\text{AE} < 100 \text{ nT}$, (b) $100 < \text{AE} < 300 \text{ nT}$ and (c) $\text{AE} > 300 \text{ nT}$. Figure from Douma et al. (2017).

339 hour relativistic microburst storm and found that the mesospheric ozone was reduced
 340 by 7 – 12% in the summer months and 12 – 20% in the winter months.

341 Furthermore, microbursts have also been estimated to have a significant impact
 342 on the outer radiation belt electrons. Radiation belt electron loss due to microbursts
 343 has been estimated to be on the order of a day (Breneman et al., 2017; Douma
 344 et al., 2019; Lorentzen et al., 2001b; O’Brien et al., 2004; Thorne et al., 2005).

345 The wave-particle interactions responsible for generating microbursts are also
 346 believed to accelerate electrons in the radiation belts. As mentioned earlier, when
 347 an electron is in resonance with a wave, energy is exchanged with the wave and
 348 the electron is either accelerated or decelerated. The signature of wave-particle
 349 acceleration been observed for radiation belt electrons (e.g. Horne et al., 2005;
 350 Meredith et al., 2002; Reeves et al., 2013). O’Brien et al. (2003) presented evidence
 351 that enhancements in chorus waves, microbursts, and radiation belt electrons are
 352 related. O’Brien et al. (2003) proposed an explanation where microburst precipitation
 353 is a side effect of electron acceleration due to chorus waves. The widely used
 354 theoretical framework to model interactions between electrons and chorus waves is

355 quasi-linear diffusion (e.g. Horne et al., 2005; Meredith et al., 2002; Summers, 2005;
 356 Summers et al., 1998; Thorne et al., 2005; Walker, 1993) which is derived in Chapter
 357 ???. Qualitatively, when a particle is resonant with a wave it can be transported in
 358 pitch angle towards the loss cone and lose energy to the wave. In contrast, if the
 359 particle is transported away from the loss cone, it gains energy from the wave.

360 The range of observed microburst energies range from a few tens of keV (e.g.
 361 Datta et al., 1997; Parks, 1967) to greater than 1 MeV (e.g. Blake et al., 1996; Greeley
 362 et al., 2019). The microburst electron flux (J) falls off in energy, and the microburst
 363 energy spectra is typically well fit to a decaying exponential

$$J(E) = J_0 e^{-E/E_0} \quad (1.23)$$

364 where J_0 is the flux at 0 keV (unphysical free parameter) and E_0 quantifies the
 365 efficiency of the scattering mechanism in energy (.e.g Datta et al., 1997; Lee et al.,
 366 2005; Parks, 1967). A small E_0 suggests that mostly low energy particles are scattered
 367 and a high E_0 suggests that the scattering mechanism scatters low and high energy
 368 electrons. Reality is a bit more messy and a high E_0 may be a signature of a scattering
 369 mechanism preferential to high energy electrons, but is hidden by the convolution of
 370 the source particles available to be scattered (typically with a falling energy spectrum)
 371 and the energy-dependent scattering efficiency.

372 The short duration of microbursts observed by a single LEO satellite has an
 373 ambiguity when interpreting what is exactly a microburst. The two possible realities
 374 are: a microburst is very small and spatially stationary so that the LEO spacecraft
 375 passes through it in less than a second. Alternatively, microbursts are spatially large
 376 with a short duration such that the microburst passes by the spacecraft in a fraction
 377 of a second. There are a few ways to distinguish between the two possible realities,

378 and each one has a unique set of advantages.

379 A high altitude balloon provides essentially a stationary view of the precipitating
 380 particles under the radiation belt footprints so a short-lived, temporal microburst can
 381 be unambiguously identified. Spatial structures, on the other hand, are difficult to
 382 identify because a balloon is essentially still on drift timescales.

383 Multi-spacecraft missions are an alternate solution which can determine if a
 384 microburst-like feature is spatial or temporal. As will be shown in this dissertation,
 385 if a microburst is observed simultaneously by two spacecraft then it is temporal and
 386 has a size greater than the spacecraft separation. On the contrary, if two spacecraft
 387 observe a microburst-like feature at different times, but at the same location, then
 388 the feature is spatial and may be a curtain (Blake and O'Brien, 2016). Both balloon
 389 and multi-spacecraft observational methods have a unique set of strengths, and this
 390 dissertation takes the multi-spacecraft approach to identify and study microbursts.

391

Scope of Research

392 This dissertation furthers our understanding of the microburst scattering
 393 mechanism by observing the scattering directly, and measuring the microburst sizes
 394 and comparing them to the size of waves near the magnetic equator where those
 395 electrons could have been scattered. Chapter ?? describes a microburst scattering
 396 event observed by NASA's Van Allen Probes which was studied in the theoretic
 397 framework of pitch angle and energy diffusion. The following two chapters will then
 398 study the size of microbursts. Chapter ?? describes a bouncing packet microburst
 399 observation made by MSU's FIREBIRD-II mission where the microburst's lower
 400 bound longitudinal and latitudinal sizes were estimated. Then Chapter ?? expands
 401 the case study from Ch. ?? to a statistical study of microburst sizes using The
 402 Aerospace Corporation's AeroCube-6 (AC6) CubeSats. In this study, a Monte Carlo

403 and analytic microburst size models were developed to account for the compounding
404 effects of random microburst sizes and locations. Lastly, Chapter ?? will summarize
405 the dissertation work and make concluding remarks regarding outstanding questions
406 in microburst physics.

Bibliography

- 408 Anderson, B., Shekhar, S., Millan, R., Crew, A., Spence, H., Klumpar, D., Blake, J.,
 409 O'Brien, T., and Turner, D. (2017). Spatial scale and duration of one microburst
 410 region on 13 August 2015. *Journal of Geophysical Research: Space Physics*.
- 411 Anderson, K. A. and Milton, D. W. (1964). Balloon observations of X rays in the
 412 auroral zone: 3. High time resolution studies. *Journal of Geophysical Research*,
 413 69(21):4457–4479.
- 414 Barcus, J., Brown, R., and Rosenberg, T. (1966). Spatial and temporal character of
 415 fast variations in auroral-zone x rays. *Journal of Geophysical Research*, 71(1):125–
 416 141.
- 417 Baumjohann, W. and Treumann, R. A. (1997). *Basic space plasma physics*. World
 418 Scientific.
- 419 Blake, J.,Looper, M., Baker, D., Nakamura, R., Klecker, B., and Hovestadt, D.
 420 (1996). New high temporal and spatial resolution measurements by sampex of the
 421 precipitation of relativistic electrons. *Advances in Space Research*, 18(8):171 – 186.
- 422 Blake, J. B. and O'Brien, T. P. (2016). Observations of small-scale latitudinal
 423 structure in energetic electron precipitation. *Journal of Geophysical Research: Space
 424 Physics*, 121(4):3031–3035. 2015JA021815.
- 425 Blum, L., Li, X., and Denton, M. (2015). Rapid MeV electron precipitation as
 426 observed by SAMPEX/HILT during high-speed stream-driven storms. *Journal of
 427 Geophysical Research: Space Physics*, 120(5):3783–3794. 2014JA020633.
- 428 Breneman, A., Crew, A., Sample, J., Klumpar, D., Johnson, A., Agapitov, O.,
 429 Shumko, M., Turner, D., Santolik, O., Wygant, J., et al. (2017). Observations
 430 directly linking relativistic electron microbursts to whistler mode chorus: Van allen
 431 probes and FIREBIRD II. *Geophysical Research Letters*.
- 432 Breneman, A. W., Halford, A., Millan, R., McCarthy, M., Fennell, J., Sample, J.,
 433 Woodger, L., Hospodarsky, G., Wygant, J. R., Cattell, C. A., et al. (2015). Global-
 434 scale coherence modulation of radiation-belt electron loss from plasmaspheric hiss.
 435 *Nature*, 523(7559):193.
- 436 Brown, R., Barcus, J., and Parsons, N. (1965). Balloon observations of auroral zone
 437 x rays in conjugate regions. 2. microbursts and pulsations. *Journal of Geophysical
 438 Research (U.S.)*.
- 439 Capannolo, L., Li, W., Ma, Q., Shen, X.-C., Zhang, X.-J., Redmon, R., Rodriguez,
 440 J., Engebretson, M., Kletzing, C., Kurth, W., et al. (2019). Energetic electron
 441 precipitation: multi-event analysis of its spatial extent during emic wave activity.
 442 *Journal of Geophysical Research: Space Physics*.

- 443 Claudepierre, S., O'Brien, T.,Looper, M., Blake, J., Fennell, J., Roeder, J.,
 444 Clemmons, J., Mazur, J., Turner, D., Reeves, G., et al. (2019). A revised look
 445 at relativistic electrons in the earth's inner radiation zone and slot region. *Journal*
 446 *of Geophysical Research: Space Physics*, 124(2):934–951.
- 447 Crew, A. B., Spence, H. E., Blake, J. B., Klumpar, D. M., Larsen, B. A., O'Brien,
 448 T. P., Driscoll, S., Handley, M., Legere, J., Longworth, S., Mashburn, K.,
 449 Mosleh, E., Ryhajlo, N., Smith, S., Springer, L., and Widholm, M. (2016). First
 450 multipoint in situ observations of electron microbursts: Initial results from the
 451 NSF FIREBIRD II mission. *Journal of Geophysical Research: Space Physics*,
 452 121(6):5272–5283. 2016JA022485.
- 453 Datta, S., Skoug, R., McCarthy, M., and Parks, G. (1997). Modeling of microburst
 454 electron precipitation using pitch angle diffusion theory. *Journal of Geophysical*
 455 *Research: Space Physics*, 102(A8):17325–17333.
- 456 Douma, E., Rodger, C., Blum, L., O'Brien, T., Clilverd, M., and Blake, J. (2019).
 457 Characteristics of relativistic microburst intensity from sampex observations.
 458 *Journal of Geophysical Research: Space Physics*.
- 459 Douma, E., Rodger, C. J., Blum, L. W., and Clilverd, M. A. (2017). Occurrence
 460 characteristics of relativistic electron microbursts from SAMPEX observations.
 461 *Journal of Geophysical Research: Space Physics*, 122(8):8096–8107. 2017JA024067.
- 462 Eastwood, J., Hietala, H., Toth, G., Phan, T., and Fujimoto, M. (2015). What
 463 controls the structure and dynamics of earths magnetosphere? *Space Science*
 464 *Reviews*, 188(1-4):251–286.
- 465 Greeley, A., Kanekal, S., Baker, D., Klecker, B., and Schiller, Q. (2019). Quantifying
 466 the contribution of microbursts to global electron loss in the radiation belts. *Journal*
 467 *of Geophysical Research: Space Physics*.
- 468 Hendry, A. T., Rodger, C. J., and Clilverd, M. A. (2017). Evidence of sub-mev
 469 emic-driven electron precipitation. *Geophysical Research Letters*, 44(3):1210–1218.
- 470 Horne, R., Glauert, S., Meredith, N., Boscher, D., Maget, V., Heynderickx, D., and
 471 Pitchford, D. (2013). Space weather impacts on satellites and forecasting the earth's
 472 electron radiation belts with spacecast. *Space Weather*, 11(4):169–186.
- 473 Horne, R. B., Thorne, R. M., Shprits, Y. Y., Meredith, N. P., Glauert, S. A., Smith,
 474 A. J., Kanekal, S. G., Baker, D. N., Engebretson, M. J., Posch, J. L., et al.
 475 (2005). Wave acceleration of electrons in the van allen radiation belts. *Nature*,
 476 437(7056):227.
- 477 Kasahara, S., Miyoshi, Y., Yokota, S., Mitani, T., Kasahara, Y., Matsuda, S.,
 478 Kumamoto, A., Matsuoka, A., Kazama, Y., Frey, H., et al. (2018). Pulsating
 479 aurora from electron scattering by chorus waves. *Nature*, 554(7692):337.

- 480 Klumpar, D., Springer, L., Mosleh, E., Mashburn, K., Berardinelli, S., Gunderson,
 481 A., Handly, M., Ryhajlo, N., Spence, H., Smith, S., Legere, J., Widholm, M.,
 482 Longworth, S., Crew, A., Larsen, B., Blake, J., and Walmsley, N. (2015). Flight
 483 system technologies enabling the twin-cubesat firebird-ii scientific mission.
- 484 Lee, J. J., Parks, G. K., Lee, E., Tsurutani, B. T., Hwang, J., Cho, K. S., Kim, K.-H.,
 485 Park, Y. D., Min, K. W., and McCarthy, M. P. (2012). Anisotropic pitch angle
 486 distribution of 100 keV microburst electrons in the loss cone: measurements from
 487 STSAT-1. *Annales Geophysicae*, 30(11):1567–1573.
- 488 Lee, J.-J., Parks, G. K., Min, K. W., Kim, H. J., Park, J., Hwang, J., McCarthy,
 489 M. P., Lee, E., Ryu, K. S., Lim, J. T., Sim, E. S., Lee, H. W., Kang, K. I., and
 490 Park, H. Y. (2005). Energy spectra of 170–360 keV electron microbursts measured
 491 by the korean STSAT-1. *Geophysical Research Letters*, 32(13). L13106.
- 492 Li, X., Selesnick, R., Schiller, Q., Zhang, K., Zhao, H., Baker, D. N., and Temerin,
 493 M. A. (2017). Measurement of electrons from albedo neutron decay and neutron
 494 density in near-earth space. *Nature*, 552(7685):382.
- 495 Lorentzen, K. R., Blake, J. B., Inan, U. S., and Bortnik, J. (2001a). Observations
 496 of relativistic electron microbursts in association with VLF chorus. *Journal of
 497 Geophysical Research: Space Physics*, 106(A4):6017–6027.
- 498 Lorentzen, K. R.,Looper, M. D., and Blake, J. B. (2001b). Relativistic electron
 499 microbursts during the GEM storms. *Geophysical Research Letters*, 28(13):2573–
 500 2576.
- 501 Lyons, L. R. and Thorne, R. M. (1973). Equilibrium structure of radiation belt
 502 electrons. *Journal of Geophysical Research*, 78(13):2142–2149.
- 503 Meredith, N., Horne, R., Summers, D., Thorne, R., Iles, R., Heynderickx, D., and
 504 Anderson, R. (2002). Evidence for acceleration of outer zone electrons to relativistic
 505 energies by whistler mode chorus. In *Annales Geophysicae*, volume 20, pages 967–
 506 979.
- 507 Millan, R. and Thorne, R. (2007). Review of radiation belt relativistic electron losses.
 508 *Journal of Atmospheric and Solar-Terrestrial Physics*, 69(3):362 – 377.
- 509 Nakamura, R., Baker, D. N., Blake, J. B., Kanekal, S., Klecker, B., and Hovestadt,
 510 D. (1995). Relativistic electron precipitation enhancements near the outer edge of
 511 the radiation belt. *Geophysical Research Letters*, 22(9):1129–1132.
- 512 Nakamura, R., Isowa, M., Kamide, Y., Baker, D., Blake, J., and Looper, M. (2000).
 513 Observations of relativistic electron microbursts in association with VLF chorus.
 514 *J. Geophys. Res.*, 105:15875–15885.

- 515 O'Brien, T., Claudepierre, S., Blake, J., Fennell, J. F., Clemons, J., Roeder, J.,
 516 Spence, H. E., Reeves, G., and Baker, D. (2014). An empirically observed pitch-
 517 angle diffusion eigenmode in the earth's electron belt near $l^* = 5.0$. *Geophysical*
 518 *Research Letters*, 41(2):251–258.
- 519 O'Brien, T., Claudepierre, S., Guild, T., Fennell, J., Turner, D., Blake, J., Clemons,
 520 J., and Roeder, J. (2016). Inner zone and slot electron radial diffusion revisited.
 521 *Geophysical Research Letters*, 43(14):7301–7310.
- 522 O'Brien, T. and Moldwin, M. (2003). Empirical plasmapause models from magnetic
 523 indices. *Geophysical Research Letters*, 30(4).
- 524 O'Brien, T. P.,Looper, M. D., and Blake, J. B. (2004). Quantification of relativistic
 525 electron microburst losses during the GEM storms. *Geophysical Research Letters*,
 526 31(4). L04802.
- 527 O'Brien, T. P., Lorentzen, K. R., Mann, I. R., Meredith, N. P., Blake, J. B., Fennell,
 528 J. F.,Looper, M. D., Milling, D. K., and Anderson, R. R. (2003). Energization of
 529 relativistic electrons in the presence of ULF power and MeV microbursts: Evidence
 530 for dual ULF and VLF acceleration. *Journal of Geophysical Research: Space*
 531 *Physics*, 108(A8).
- 532 Ozaki, M., Miyoshi, Y., Shiokawa, K., Hosokawa, K., Oyama, S.-i., Kataoka, R.,
 533 Ebihara, Y., Ogawa, Y., Kasahara, Y., Yagitani, S., et al. (2019). Visualization of
 534 rapid electron precipitation via chorus element wave–particle interactions. *Nature*
 535 *communications*, 10(1):257.
- 536 Parks, G. K. (1967). Spatial characteristics of auroral-zone X-ray microbursts. *Journal*
 537 *of Geophysical Research*, 72(1):215–226.
- 538 Reeves, G., Spence, H. E., Henderson, M., Morley, S., Friedel, R., Funsten, H., Baker,
 539 D., Kanekal, S., Blake, J., Fennell, J., et al. (2013). Electron acceleration in the
 540 heart of the van allen radiation belts. *Science*, 341(6149):991–994.
- 541 Reeves, G. D., McAdams, K. L., Friedel, R. H. W., and O'Brien, T. P. (2003). Ac-
 542 celeration and loss of relativistic electrons during geomagnetic storms. *Geophysical*
 543 *Research Letters*, 30(10):n/a–n/a. 1529.
- 544 Schulz, M. and Lanzerotti, L. J. (1974). *Particle Diffusion in the Radiation Belts*.
 545 Springer.
- 546 Seppälä, A., Douma, E., Rodger, C., Verronen, P., Clilverd, M. A., and Bortnik, J.
 547 (2018). Relativistic electron microburst events: Modeling the atmospheric impact.
 548 *Geophysical Research Letters*, 45(2):1141–1147.

- 549 Spence, H. E., Blake, J. B., Crew, A. B., Driscoll, S., Klumpar, D. M., Larsen,
 550 B. A., Legere, J., Longworth, S., Mosleh, E., O'Brien, T. P., Smith, S., Springer,
 551 L., and Widholm, M. (2012). Focusing on size and energy dependence of electron
 552 microbursts from the van allen radiation belts. *Space Weather*, 10(11).
- 553 Summers, D. (2005). Quasi-linear diffusion coefficients for field-aligned electro-
 554 magnetic waves with applications to the magnetosphere. *Journal of Geophysical
 555 Research: Space Physics*, 110(A8):n/a–n/a. A08213.
- 556 Summers, D., Thorne, R. M., and Xiao, F. (1998). Relativistic theory of wave-particle
 557 resonant diffusion with application to electron acceleration in the magnetosphere.
 558 *Journal of Geophysical Research: Space Physics*, 103(A9):20487–20500.
- 559 Thorne, R. M., O'Brien, T. P., Shprits, Y. Y., Summers, D., and Horne, R. B. (2005).
 560 Timescale for MeV electron microburst loss during geomagnetic storms. *Journal
 561 of Geophysical Research: Space Physics*, 110(A9). A09202.
- 562 Trefall, H., Bjordal, J., Ullaland, S., and Stadsnes, J. (1966). On the extension of
 563 auroral-zone x-ray microbursts. *Journal of Atmospheric and Terrestrial Physics*,
 564 28(2):225–233.
- 565 Tsurutani, B. T. and Lakhina, G. S. (1997). Some basic concepts of wave-particle
 566 interactions in collisionless plasmas. *Reviews of Geophysics*, 35(4):491–501.
- 567 Ukhorskiy, A. Y., Anderson, B. J., Brandt, P. C., and Tsyganenko, N. A. (2006).
 568 Storm time evolution of the outer radiation belt: Transport and losses. *Journal of
 569 Geophysical Research: Space Physics*, 111(A11):n/a–n/a. A11S03.
- 570 Van Allen, J. A. (1959). The geomagnetically trapped corpuscular radiation. *Journal
 571 of Geophysical Research*, 64(11):1683–1689.
- 572 Vernov, S. and Chudakov, A. (1960). Investigation of radiation in outer space. In
 573 *International Cosmic Ray Conference*, volume 3, page 19.
- 574 Walker, A. D. M. (1993). *Plasma waves in the magnetosphere*, volume 24. Springer
 575 Science & Business Media.